JOURNAL OF THEORETICAL
AND APPLIED MECHANICS
https://doi.org/10.15632/jtam-pl/215405
ONLINE FIRST

PHYSICS-INFORMED NEURAL NETWORKS FOR INHOMOGENEOUS SWELLING ANALYSIS OF DUAL-LAYER GELS WITH CHAIN ENTANGLEMENT EFFECTS

Hengdi SU, Feifei SONG, Chengjin SUN, Jianjun ZHANG*

College of Information and Management Science, Henan Agricultural University, Zhengzhou, China
*corresponding author, *zjj@henau.edu.cn*

A field theory incorporating Edwards–Vilgis slip-link elasticity with Flory–Huggins mixing is developed for dual-layer gels containing rigid cores, capturing chain entanglement effects neglected by Neo–Hookean models. Physics-informed neural networks (PINNs) transform complexities of handling interfacial constraints into a neural network optimization problem, thereby reducing both algorithmic complexity and implementation requirements. Systematic parametric studies demonstrate that micromaterial parameters critically govern stress distributions, solvent concentration profiles, and swelling behavior. The framework enables precise control of target solvent concentrations and equilibrium configurations through optimal micromaterial parameter selection and thickness ratio design in dual-layer spherical gel systems.

Keywords: dual-layer gels; physics-informed neural networks; chain entanglement.

1. Introduction

Upon contact with a network of hydrophilic crosslinked polymer chains, solution molecules become enmeshed within the network due to intermolecular attractions, leading to volumetric expansion through solution imbibition. This hydrated, expanded state is characteristically termed a polymeric gel, which exhibits high solvent uptake and substantial swelling ratios, enabling applications in tissue engineering (Khan *et al.*, 2024), self-folding structures (Zhao *et al.*, 2021), and soft robotics (López-Díaz *et al.*, 2024). Their programmable deformation capabilities and tunable mechanical properties establish gels as essential materials for interdisciplinary technological advancement. In many applications, gels are commonly interfaced with diverse materials to create composite gel systems (Yang *et al.*, 2020), including gel-metal, gel-gel, and gel-tissue interfaces. Spherical gel shells coating a rigid core have been extensively studied due to their broad utility in soft matter and biomedical applications (Ballauff & Lu, 2007). However, single-layer gels often lack the functional versatility required to satisfy multiple design criteria. In contrast, multilayer gels offer a compelling solution by enabling spatially tailored properties across distinct layers. For example, Yan *et al.* (2021) developed a chitosan/silver nanoparticle multilayer gel that exploits chitosan's capacity to adsorb and stabilize metal salts, coupled with the antimicrobial action arising from silver-ion diffusion. In gel micro-valves, a relatively stiff outer layer is particularly beneficial, as it induces compressive radial stresses that stabilize the core-shell structure and reduce wear and degradation of the softer inner gel. The preparation, characterization and application of multilayer gels have been comprehensively reviewed by (Jin *et al.*, 2021).

When subjected to external mechanical constraints during equilibration, these gels typically develop inhomogeneous and anisotropic swelling deformations characterized by non-uniform solvent distribution. To better harness these gel systems, many theories have been established to elucidate and interpret the swelling behavior of gel systems under diverse mechanical con-

straints. Zhao *et al.* (2008) characterized the inhomogeneous and anisotropic equilibrium behavior in spherical gel shells adhered to rigid core materials, demonstrating how mechanical constraints in core-shell architectures influence swelling patterns. Morimoto and Ashida (2015) investigated bilayer gel systems comprising two thermally responsive hydrogel layers with differential swelling properties, observing spontaneous bending upon immersion in solution at specific temperatures. Ahmadi *et al.* (2020) conducted quantitative analyses of displacement fields, stress distributions, and solvent concentration gradients in bi-layered spherical hydrogels bonded to rigid cores. Wu and Zhong (2013) systematically evaluated the swelling equilibrium states of core-shell-coating gel structures.

The aforementioned theoretical frameworks characterizing deformation phenomena of gel systems are predominantly formulated within continuum mechanics principles, employing the Flory–Rehner free energy function as the fundamental constitutive relation that governs the material response. This idealized formulation integrates the Gaussian chain model to characterize the elastic response of polymer networks with the Flory–Huggins solution theory to account for polymer-solvent mixing energetics. Despite its widespread application in modeling various chemo-mechanical coupling phenomena in polymer gels, the classical Flory–Rehner model employs a Neo–Hookean representation for the network stretching free energy, which notably neglects chain extensibility limitations. To address this limitation, Chester and Anand (2010) developed a refined theory based on non-Gaussian statistical mechanics of polymer chains. While this non-Gaussian approach offers a more physically realistic representation compared to Gaussian statistics, it fails to incorporate the significant effects of chain entanglements – a crucial consideration given that these entanglements are ubiquitous in actual gel networks due to the fundamental uncrossability of network chains. These uncrosslinked polymer chain interactions, termed slip-links, represent inevitable structural features in hydrogel preparation, as the formation of defect-free chemically cross-linked polymer networks remains practically unattainable. Numerous models have been developed to characterize the entanglement effects in cross-linked polymer networks. Among these, the Edwards–Vilgis slip-link model (Edwards & Vilgis, 1986) has been shown to exhibit the strongest agreement with experimental results, as demonstrated by comparative analyses with experimental data (Urayama *et al.*, 2003). Yan and Jin (2012) propose a novel hybrid free energy function for polymeric gels that combines the Edwards–Vilgis slip-link model of elasticity with the Flory–Huggins mixing formulation, by which some elementary deformation scenarios in single-component gel segments are carried out, showing good agreement with experimental results.

In this work, we systematically investigate the influence of entanglements on the inhomogeneous and anisotropic swelling behavior of dual-layer gels containing rigid cores, and establish a rigorous framework for the design and optimization of micromechanical properties and thickness ratios in dual-layer gel systems, enabling precise control over target solvent concentrations and sealing-induced stresses.

Traditionally, complex phenomena in gel systems have been analyzed using finite element methods. However, these conventional numerical approaches require iterative solution procedures when addressing differential equations with interface continuity conditions, which necessitate the successive resolution of the governing equations at each iteration step, resulting in increased computational complexity and implementation overhead (Abdolahi *et al.*, 2017). Furthermore, these mesh-based methods necessitate the discretization of the computational domain into mesh points, approximating solutions at these discrete locations while yielding results with limited differentiability.

Recent years have witnessed a transformative application of artificial neural networks (ANNs) – also known as deep neural networks (DNNs) or deep learning (DL) – across numerous disciplines including image classification, handwriting recognition, speech processing, and computer vision. These computational paradigms have subsequently emerged in scientific computing, particularly for solving partial differential equations (PDEs). Among these approaches, physics-

informed neural networks (PINNs) have become a prominent methodology for training DNN-based solutions to PDEs and have been successfully applied to various engineering challenges (Diao *et al.*, 2023; Raissi *et al.*, 2019). In our prior work (Su *et al.*, 2021; Su *et al.*, 2022), we employed a deep learning approach to model the swelling behavior of core-shell gel responding to environmental stimuli. The inherent flexibility in defining DNNs, coupled with significant advances in algorithmic efficiency, positions DNNs as a compelling alternative for PDE solution approximation.

In this study, we employ PINNs to investigate the swelling behavior of dual-layer gels. The interface continuity conditions are elegantly incorporated into the loss function alongside other governing physical laws, thereby transforming the complexities of solving governing equations with interface continuity conditions into a neural network optimization problem. This approach represents a significant paradigm shift in computational mechanics, where traditional numerical challenges are reframed within the well-established domain of deep learning optimization techniques. Furthermore, PINNs generate closed-form, analytically differentiable solutions – a substantial advantage for subsequent calculations compared to the discrete or limited-differentiability solutions offered by conventional methods. Moreover, the near-mathematical syntax facilitated by TensorFlow or PyTorch frameworks enhances both implementation clarity and accessibility. Last but not least, PINNs efficiently leverage modern parallel computing architectures, enabling effective deployment across multiple graphics processing units (GPUs) or tensor processing units (TPUs).

The remainder of this paper is organized as follows: Section 2 presents a comprehensive theoretical framework for modeling the inhomogeneous and anisotropic swelling behavior of dual-layer spherical gels containing rigid cores, with particular emphasis on the incorporation of chain entanglement effects through the Edwards–Vilgis slip-link model. Section 3 introduces the PINN methodology specifically adapted for solving the dual-layer gel problem. Section 4 provides a systematic investigation of the influence of micromaterial parameters on the mechanical behavior of dual-layer gel systems.

2. Model description

2.1. Kinematic relations and equilibrium equations

In Fig. 1, we present a schematic illustration of inhomogeneous swelling deformations in a dual-layer spherical gel system with distinct micromaterial parameters. The reference state (Fig. 1a) depicts two stress-free dry spherical gels perfectly adhered to a rigid core. Gel 1 occupies the inner layer region $B^{(1)}$ between radii R_{in} and R_{inter}, while gel 2 forms the outer layer region between R_{inter} and R_{out}. Let $\boldsymbol{\chi}^{(s)}$, $s = 1, 2$ be first-order tensor fields denoting the deformation mappings from the regions $B^{(s)}$ into their deformed states occupying the regions $\mathcal{B}^{(s)}$ (throughout the subsequent analysis, where the superscript s appears without explicit specification of its range, it is understood to take values $s = 1, 2$, corresponding to the respective gel layers). Upon immersion in a solvent with chemical potential $\mu = 0$, the system reaches equilibrium with

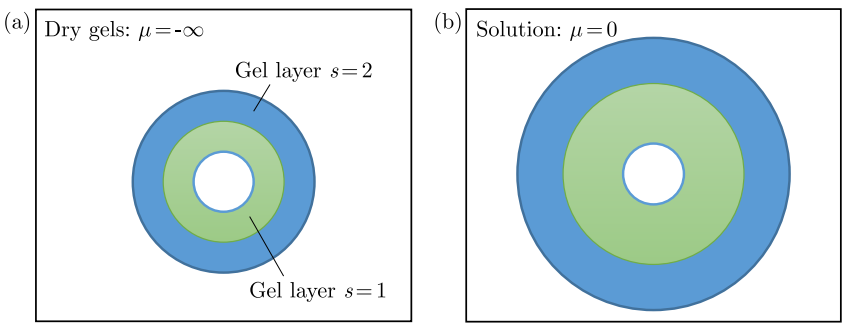

Fig. 1. Schematic illustration of a dual-layer gel containing a rigid core: (a) fluid-free and stress-free state serving as the reference configuration; (b) swollen state reaches equilibrium with the surrounding solution.

the external solution (Fig. 1b). Utilizing the orthogonal Cartesian basis vectors $\mathbf{e}_i$ $(i = 1, 2, 3)$, we formulate a spherical coordinate system $\mathbf{e}_R$, $\mathbf{e}_\theta$, and $\mathbf{e}_\varphi$. The deformation gradient can be represented by

$$\mathbf{F}^{(s)} = \boldsymbol{\chi}^{(s)} \otimes \nabla = \frac{\mathrm{d}r^{(s)}}{\mathrm{d}R^{(s)}} \mathbf{e}_R \otimes \mathbf{e}_R + \frac{r^{(s)}}{R^{(s)}} \mathbf{e}_\theta \otimes \mathbf{e}_\theta + \frac{r^{(s)}}{R^{(s)}} \mathbf{e}_\varphi \otimes \mathbf{e}_\varphi, \tag{2.1}$$

where $r^{(s)}$ represents the radial coordinate of the bilayer gels in a swollen state. The principal stretches in the radial and hoop directions are, respectively, defined as

$$\lambda_R^{(s)} = \frac{\mathrm{d}r^{(s)}}{\mathrm{d}R^{(s)}}, \qquad \lambda_\theta^{(s)} = \lambda_\varphi^{(s)} = \frac{r^{(s)}}{R^{(s)}}. \tag{2.2}$$

The incompressibility of all molecular constituents within the gel system yields a volumetric constraint wherein the total gel volume equals the sum of the dry polymer network volume and the volume of absorbed solvent molecules. This relationship can be mathematically expressed as

$$1 + vC^{(s)} = \det \mathbf{F}^{(s)} = J^{(s)}, \tag{2.3}$$

where v is the volume per solvent molecule, and $C^{(s)}$ denotes the solvent concentration in gel s.

The swelling mechanics of this structure can be characterized as follows: near the core-gel interface, the rigid core constrains hoop direction swelling while permitting radial stretching. Due to the dissimilar micromaterial parameters of gel 1 and gel 2, their respective swelling behaviors differ significantly, generating interfacial forces between the two layers. These forces either promote separation or cohesion between the gels. However, since the two gel layers are perfectly bonded, they must accommodate each other's deformation, maintaining identical radial displacement magnitudes at their interface. Phenomena such as asymmetric deformations, interfacial debonding, and fracture are beyond the scope of the current research.

In the absence of body forces, the conservation of linear momentum reduces to the equilibrium equations:

$$\mathbf{P}^{(s)} \cdot \nabla = \mathbf{0}, \tag{2.4}$$

where $\mathbf{P}^{(s)}$ represents the nominal stress tensor, also known as the first Piola–Kirchhoff stress tensor.

The nominal stress tensor in each gel layer, expressed in the spherical coordinate system, takes the form:

$$\mathbf{P}^{(s)} = P_R^{(s)} \mathbf{e}_R \otimes \mathbf{e}_R + P_\theta^{(s)} \mathbf{e}_\theta \otimes \mathbf{e}_\theta + P_\varphi^{(s)} \mathbf{e}_\varphi \otimes \mathbf{e}_\varphi. \tag{2.5}$$

Upon substitution of Eq. (2.5) into the equilibrium equation (2.4) and simplification, we obtain the governing differential equation:

$$\frac{\mathrm{d}P_R^{(s)}}{\mathrm{d}R^{(s)}} + \frac{2}{R^{(s)}} \left(P_R^{(s)} - P_\theta^{(s)} \right) = 0. \tag{2.6}$$

Under the assumption of spherically symmetric deformations and perfectly bonded interfaces between the core-gel and gel-gel, the boundary conditions can be formulated as

$$\lambda_\theta^{(1)}(R_{\mathrm{in}}) = 1, \qquad P_R^{(2)}(R_{\mathrm{out}}) = 0, \tag{2.7}$$

including the following interface continuity conditions:

$$P_R^{(1)}(R_{\mathrm{inter}}) = P_R^{(2)}(R_{\mathrm{inter}}), \qquad \lambda_\theta^{(1)}(R_{\mathrm{inter}}) = \lambda_\theta^{(2)}(R_{\mathrm{inter}}). \tag{2.8}$$

2.2. Constitutive equations

Let $W^{(s)}$ denote the Helmholtz free energy density of the gel s. Assuming the gel s is in equilibrium state characterized by the displacement field $\boldsymbol{\chi}^{(s)}$ and solvent concentration field $C^{(s)}$,

thermodynamic principles stipulate that the variation in the gel's free energy must equate to the work exerted by external mechanical force and solvent, as encapsulated by

$$\int_{B^{(s)}} \delta W^{(s)} \, \mathrm{d}V = \int_{\partial B^{(s)}} \mathbf{P}^{(s)} \mathbf{N}^{(s)} \delta \boldsymbol{\chi}^{(s)} \, \mathrm{d}A + \mu \int_{B^{(s)}} \delta C^{(s)} \, \mathrm{d}V, \tag{2.9}$$

where $\mathbf{N}^{(s)}$ denotes the unit vector normal to the boundary $\partial B^{(s)}$ of the reference configuration $B^{(s)}$.

Under the assumption that the free energy density function $W^{(s)}$ depends on the deformation gradient $\mathbf{F}^{(s)}$ and solvent concentration $C^{(s)}$, applying the divergence theorem to Eq. (2.9) yields:

$$\int_{B^{(s)}} \left(\frac{\partial W^{(s)}}{\partial \mathbf{F}^{(s)}} - \mathbf{P}^{(s)} \right) : \delta \mathbf{F}^{(s)} \, \mathrm{d}V + \int_{B^{(s)}} \left(\mathbf{P}^{(s)} \cdot \nabla \right) \delta \boldsymbol{\chi}^{(s)} \, \mathrm{d}V + \int_{B^{(s)}} \left(\frac{\partial W^{(s)}}{\partial C^{(s)}} - \mu \right) \delta C^{(s)} \, \mathrm{d}V = 0. \tag{2.10}$$

The middle term in Eq. (2.10) vanishes upon application of the equilibrium Eq. (2.4). Consequently, Eq. (2.10) boils down to the constitutive equations:

$$\frac{\partial W^{(s)}}{\partial \mathbf{F}^{(s)}} = \mathbf{P}^{(s)}, \qquad \frac{\partial W^{(s)}}{\partial C^{(s)}} = \mu. \tag{2.11}$$

Following Flory and Rehner (1943), the Helmholtz free energy of the gel takes the form:

$$W^{(s)} = W^{(s)}_{\mathrm{mix}} + W^{(s)}_{\mathrm{str}}, \tag{2.12}$$

where $W^{(s)}_{\mathrm{mix}}$ arises from mixing the polymers with the solvent molecules and $W^{(s)}_{\mathrm{str}}$ from stretching the gel network.

Flory (1942) and Huggins (1941) developed the expression for the free energy of mixing:

$$W^{(s)}_{\mathrm{mix}} = -\frac{kT}{v} \left(v C^{(s)} \ln \left(1 + \frac{1}{v C^{(s)}} \right) + \frac{\chi}{1 + v C^{(s)}} \right), \tag{2.13}$$

where χ represents a dimensionless parameter quantifying the enthalpy of mixing and kT the temperature in the unit of energy. For good solvents, the parameter χ typically falls within the range of 0.1 to 0.5. In our subsequent numerical calculations, we will set $\chi = 0.1$.

Including the molecular incompressibility constraint, the free energy of mixing can be reformulated as

$$W^{(s)}_{\mathrm{mix}} = -\frac{kT}{v} \left[(J^{(s)} - 1) \log \frac{J^{(s)}}{J^{(s)} - 1} + \frac{\chi}{J^{(s)}} \right]. \tag{2.14}$$

Taking into account the effect of polymer chain entanglements (Edwards & Vilgis, 1986), the Helmholtz free energy contribution attributable to the stretching of the network is formulated as

$$\begin{aligned} W^{(s)}_{\mathrm{str}} = {} & \frac{1}{2} N^{(s)}_s kT \ln \left(1 - \left(\alpha^{(s)} \right)^2 \sum \left(\lambda^{(s)}_i \right)^2 \right) \\ & + \frac{1}{2} N^{(s)}_c kT \left[\frac{\left(1 - \left(\alpha^{(s)} \right)^2 \right) \sum \left(\lambda^{(s)}_i \right)^2}{1 - \left(\alpha^{(s)} \right)^2 \sum \left(\lambda^{(s)}_i \right)^2} + \ln \left(1 - \left(\alpha^{(s)} \right)^2 \sum \left(\lambda^{(s)}_i \right)^2 \right) \right] \\ & + \frac{1}{2} N^{(s)}_s kT \sum \left\{ \frac{\left(\lambda^{(s)}_i \right)^2 \left(1 + \eta^{(s)} \right) \left(1 - \left(\alpha^{(s)} \right)^2 \right)}{\left(1 + \eta^{(s)} \left(\lambda^{(s)}_i \right)^2 \right) \left(1 - \left(\alpha^{(s)} \right)^2 \sum \left(\lambda^{(s)}_i \right)^2 \right)} + \ln \left(1 + \eta^{(s)} \left(\lambda^{(s)}_i \right)^2 \right) \right\}, \end{aligned} \tag{2.15}$$

where $N_c^{(s)}$ and $N_s^{(s)}$ denote the crosslink and slip-link concentrations, respectively, $\alpha^{(s)}$ characterizes the inextensibility parameter, $\eta^{(s)}$ is the slippage parameter, and $\lambda_i^{(s)}$ $(i = 1, 2, 3)$ represent the principal stretches.

Let $\mathbf{C^{(s)}} = \left(\mathbf{F}^{(s)}\right)^T \mathbf{F^{(s)}}$ be the right Cauchy–Green deformation tensor. The principal invariants of $\mathbf{C^{(s)}}$ can be written as

$$\begin{aligned} I_1^{(s)} &= \left(\lambda_1^{(s)}\right)^2 + \left(\lambda_2^{(s)}\right)^2 + \left(\lambda_3^{(s)}\right)^2, \\ I_2^{(s)} &= \left(\lambda_1^{(s)}\right)^2 \left(\lambda_2^{(s)}\right)^2 + \left(\lambda_2^{(s)}\right)^2 \left(\lambda_3^{(s)}\right)^2 + \left(\lambda_3^{(s)}\right)^2 \left(\lambda_1^{(s)}\right)^2, \\ I_3^{(s)} &= \left(\lambda_1^{(s)}\right)^2 \left(\lambda_2^{(s)}\right)^2 \left(\lambda_3^{(s)}\right)^2 = \left(J^{(s)}\right)^2. \end{aligned} \tag{2.16}$$

Combining Eqs. (2.15) and (2.16) yields

$$\begin{aligned} W_{\mathrm{str}}^{(s)}\left(I_1^{(s)}, I_2^{(s)}, J^{(s)}\right) &= \frac{1}{2} N_c^{(s)} kT \left[\frac{(1-(\alpha^{(s)})^2) I_1^{(s)}}{1-(\alpha^{(s)})^2 I_1^{(s)}} + \ln(1-(\alpha^{(s)})^2 I_1^{(s)})\right] \\ &+ \frac{1}{2} N_s^{(s)} kT \ln\left(\left(1+\eta^{(s)} I_1^{(s)} + (\eta^{(s)})^2 I_2^{(s)} + (\eta^{(s)})^3 (J^{(s)})^2\right)\left(1-(\alpha^{(s)})^2 I_1^{(s)}\right)\right] \\ &+ \frac{1}{2} N_s^{(s)} kT \left[\left(\frac{I_1^{(s)} + 2\eta^{(s)} I_2^{(s)} + 3(\eta^{(s)})^2 (J^{(s)})^2}{1+\eta^{(s)} I_1^{(s)} + (\eta^{(s)})^2 I_2^{(s)} + (\eta^{(s)})^3 (J^{(s)})^2}\right)\left(\frac{\left(1+\eta^{(s)}\right)\left(1-(\alpha^{(s)})^2\right)}{1-(\alpha^{(s)})^2 I_1^{(s)}}\right)\right]. \end{aligned} \tag{2.17}$$

Applying the Legendre transformation to the Helmholtz free energy yields

$$\widehat{W}^{(s)} = W^{(s)} - \mu C^{(s)}. \tag{2.18}$$

Thus, the constitutive Eqs. (2.11) can be rewritten as

$$\mathbf{P}^{(s)} = \frac{\partial \widehat{W}^{(s)}}{\partial \mathbf{F}^{(s)}}, \qquad C^{(s)} = -\frac{\partial \widehat{W}^{(s)}}{\partial \mu}. \tag{2.19}$$

By setting the chemical potential to zero and integrating Eqs. (2.18) and (2.19), we obtain

$$\begin{aligned} \mathbf{P}^{(s)} &= \frac{\partial \widehat{W}^{(s)}}{\partial \mathbf{F}^{(s)}} = \frac{\partial \widehat{W}^{(s)}}{\partial I_1^{(s)}} \frac{\partial I_1^{(s)}}{\partial \mathbf{C}^{(s)}} : \frac{\partial \mathbf{C}^{(s)}}{\partial \mathbf{F}^{(s)}} + \frac{\partial \widehat{W}^{(s)}}{\partial I_2^{(s)}} \frac{\partial I_2^{(s)}}{\partial \mathbf{C}^{(s)}} : \frac{\partial \mathbf{C}^{(s)}}{\partial \mathbf{F}^{(s)}} + \frac{\partial \widehat{W}^{(s)}}{\partial J^{(s)}} \frac{\partial J^{(s)}}{\partial \mathbf{F}^{(s)}} \\ &= 2\left[\frac{\partial \widehat{W}^{(s)}}{\partial I_1^{(s)}} \mathbf{F}^{(s)} + \frac{\partial \widehat{W}^{(s)}}{\partial I_2^{(s)}} \left(I_1^{(s)} \mathbf{F}^{(s)} - \mathbf{F}^{(s)} (\mathbf{C}^{(s)})^T\right) + \frac{\partial \widehat{W}^{(s)}}{\partial J^{(s)}} \frac{1}{2} J^{(s)} (\mathbf{F}^{(s)})^{-T}\right]. \end{aligned} \tag{2.20}$$

3. Physics-informed neural networks

As shown in Fig. 2, two DNNs serve as ansatz functions to approximate the stretch fields within the bilayer gel system. The input layer receives position coordinates $R^{(s)}$, while the output layer yields the corresponding radial and hoop stretches, $\lambda_R^{(s)}$ and$\lambda_\theta^{(s)}$, respectively (without causing notational ambiguity, we still use the notations $\lambda_R^{(s)}$ and $\lambda_\theta^{(s)}$ to represent their DNN ansatzes in this section).

Each DNN architecture incorporates six hidden layers, with each layer containing 20 neurons and employing hyperbolic tangent activation functions. The output layer utilizes linear activation

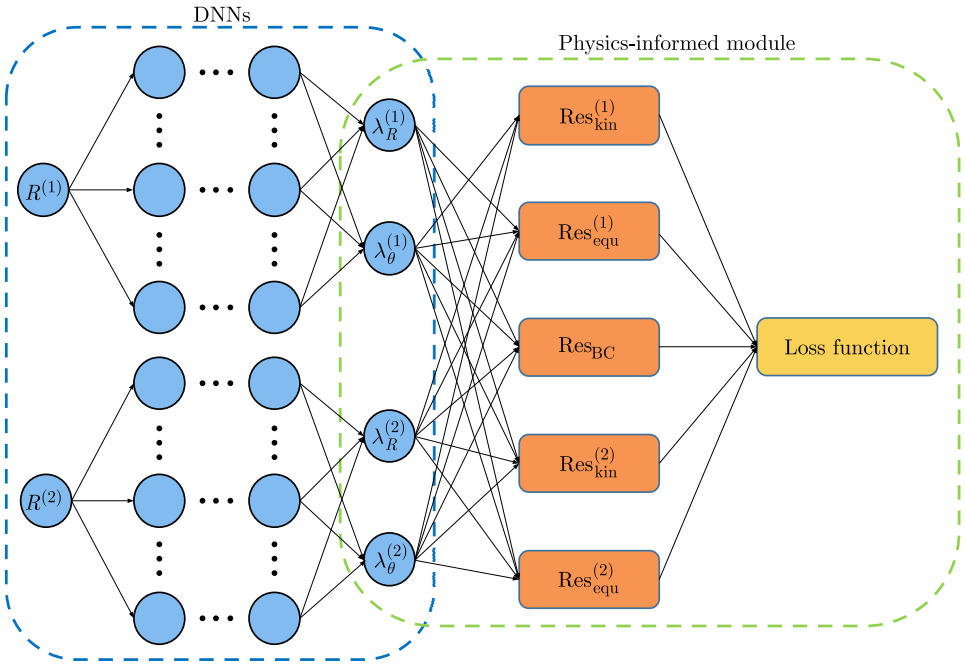

Fig. 2. Architecture of PINNs composed of DNNs and physics-informed module.

to ensure unbounded stretch predictions. Denoting the s-th DNN system as $\mathcal{N}^{(s)}$, the primary field variables (solutions) of the mechanical problem are expressed as

$$\left[\lambda_R^{(s)}, \lambda_\theta^{(s)}\right]^T = \mathcal{N}^{(s)}\left(R^{(s)}; \mathbf{W}^{(s)}\right), \tag{3.1}$$

where $\mathbf{W}^{(s)}$ represents the collection of trainable weights and biases associated with the s-th DNN.

The residual terms for the kinematic relations and equilibrium equations are formulated as

$$\begin{aligned} \mathrm{Res}_{\mathrm{kin}}^{(s)} &= \lambda_R^{(s)} - \lambda_\theta^{(s)} - R^{(s)} \frac{\mathrm{d}\lambda_\theta^{(s)}}{\mathrm{d}R^{(s)}}, \\ \mathrm{Res}_{\mathrm{equ}}^{(s)} &= \frac{\mathrm{d}P_R^{(s)}}{\mathrm{d}R^{(s)}} + \frac{2}{R^{(s)}}\left(P_R^{(s)} - P_\theta^{(s)}\right), \end{aligned} \tag{3.2}$$

where the stress components $P_R^{(s)}$ and $P_\theta^{(s)}$ are determined by substituting the DNN predictions $\lambda_R^{(s)}$ and $\lambda_\theta^{(s)}$ into the constitutive relations. The spatial derivatives of the DNN predictions are computed using automatic differentiation capabilities within the TensorFlow framework.

In conventional supervised learning paradigms, prediction accuracy is fundamentally constrained by training data availability. To mitigate this limitation, physics-informed approaches have been developed that incorporate governing physical laws as constraints. These constraints are enforced through penalty terms in the loss function, which regularize the solution by penalizing predictions that violate fundamental physical principles.

The physics-informed module in Fig. 2 systematically encodes prior knowledge, including kinematic relations, equilibrium equations, and boundary conditions, into the composite loss function:

$$\mathrm{Loss} = \mathrm{Loss}_{\mathrm{kin}}^{(1)} + \mathrm{Loss}_{\mathrm{equ}}^{(1)} + \mathrm{Loss}_{\mathrm{kin}}^{(2)} + \mathrm{Loss}_{\mathrm{equ}}^{(2)} + \mathrm{Loss}_{\mathrm{BC}}, \tag{3.3}$$

where $\mathrm{Loss}_{\mathrm{kin}}^{(s)}$ and $\mathrm{Loss}_{\mathrm{equ}}^{(s)}$ represent loss contributions from kinematic relations and equilibrium equations for the s-th gel layer, respectively, and $\mathrm{Loss}_{\mathrm{BC}}$ encompasses boundary condition constraints, including interface continuity requirements. The conventional numerical methods

encounter considerable inconvenience in handling these interface continuity conditions. In the present work, these conditions are directly encoded into the physics-informed neural network (PINN) framework, thereby transferring the complexities to the process of minimizing the associated loss function.

The individual loss terms are evaluated using mean square error formulations:

$$\begin{aligned}
\mathrm{Loss}_{\mathrm{kin}}^{(s)} &= \frac{1}{N^{(s)}}\sum_{i=1}^{N^{(s)}}\left|\mathrm{Res}_{\mathrm{kin}}^{(s)}(R_i^{(s)};\mathbf{W}^{(s)})\right|^2,\\
\mathrm{Loss}_{\mathrm{geo}}^{(s)} &= \frac{1}{N^{(s)}}\sum_{i=1}^{N^{(s)}}\left|\mathrm{Res}_{\mathrm{geo}}^{(s)}(R_i^{(s)};\mathbf{W}^{(s)})\right|^2,\\
\mathrm{Loss}_{\mathrm{BC}} &= \left|\lambda_\theta^{(1)}(R_{\mathrm{in}})-1\right|^2+\left|P_R^{(2)}(R_{\mathrm{out}})\right|^2+\left|P_R^{(1)}(R_{\mathrm{inter}})-P_R^{(2)}(R_{\mathrm{inter}})\right|^2\\
&\quad+\left|\lambda_\theta^{(1)}(R_{\mathrm{inter}})-\lambda_\theta^{(2)}(R_{\mathrm{inter}})\right|^2,
\end{aligned}\tag{3.4}$$

where $\left\{R_i^{(s)}\right\}_{i=1}^{N^{(s)}}$ denotes the set of collocation points for training the s-th neural network.

The composite loss function is minimized using the Adam optimization algorithm, a gradient-based adaptive learning rate method implemented within the TensorFlow computational environment. During the training process, primary variables $\lambda_R^{(s)}$ and $\lambda_\theta^{(s)}$ that deviate from prescribed physical constraints are penalized, thereby guiding the DNN approximations toward physically consistent results. This approach ultimately yields DNN-based solutions that satisfy the underlying physics constraints.

To enable a comparison with the PINN result, we computed a classical numerical solution using the shooting method. In the absence of entanglements ($N_s^{(s)} = \alpha^{(s)} = \eta^{(s)} = 0$), we set $vN_c^{(1)} = 0.009$ and $vN_c^{(2)} = 0.001$. We initially assume $\lambda_R^{(1)}(R_{\mathrm{in}}) = x$. Combined with the boundary condition $r^{(1)}(R_{\mathrm{in}}) = R_{\mathrm{in}}$, we solve Eq. (2.6) for $s = 1$. The solution yields $r^{(2)}(R_{\mathrm{inter}})$, which is equal to $r^{(1)}(R_{\mathrm{inter}})$. Combined with $P_R^{(2)}(R_{\mathrm{out}}) = 0$, we then solve Eq. (2.6) for $s = 2$. Finally, a root-finding algorithm adjusts the initial assumption x until the interface pressure mismatch $P_R^{(1)}(R_{\mathrm{inter}}) - P_R^{(2)}(R_{\mathrm{inter}})$ is minimized. As shown in Fig. 3, the shooting method results demonstrate good agreement with the PINN predictions.

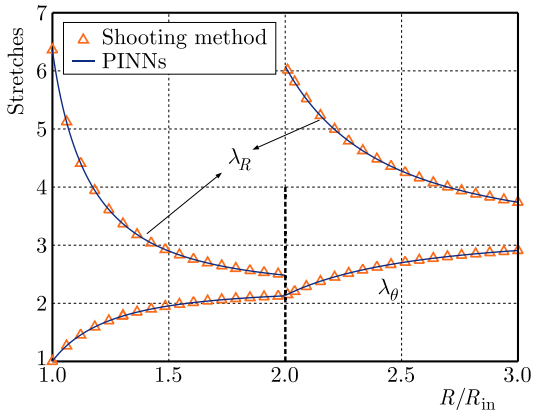

Fig. 3. Comparison of results obtained using PINNs and the shooting method.

4. Results and discussion

In this section, PINNs are employed to investigate the influence of micromaterial parameters on the inhomogeneous deformation, stress distribution, and solvent concentration in dual-layer spherical gels at equilibrium.

To examine the effect of slip-links, we maintain constant total concentrations of cross-links and slip-links in both gel layers, such that $vN_s^{(s)} + vN_c^{(s)} = 0.01$ for $s = 1, 2$, while varying the slip-link fraction defined as $\mathcal{K}^{(s)} = N_s^{(s)}/(N_s^{(s)} + N_c^{(s)})$. The inextensibility and slippage parameters are held constant at $\alpha^{(s)} = 0.1$ and $\eta^{(s)} = 0.1$ for $s = 1, 2$, respectively. Figure 4 illustrates the effects of the slip-link fraction on the radial and hoop stretches and normalized stresses when the dual-layer gels reach equilibrium. When the slip-link fractions in both layers are equal ($\mathcal{K}^{(1)} = \mathcal{K}^{(2)}$), the dual-layer system reduces to a single gel layer case, resulting in smooth stretch and stress functions. The upper panels of Fig. 4 demonstrate that near the rigid core, the hoop stretch remains constant due to core constraints, while the radial stretch increases substantially. With increasing distance from the core, the hoop and radial stretches converge. Moreover, the increasing slip-link fraction enhances both radial and hoop stretches. The lower panels reveal that near the core, the radial stress is tensile and the hoop stress is compressive due to core constraints. Both stresses diminish toward the outer surface, and their magnitudes decrease with the increasing slip-link fraction. When the slip-link fractions differ between layers ($\mathcal{K}^{(1)} \neq \mathcal{K}^{(2)}$), the behavior changes markedly. The radial stretch function exhibits discontinuity at the gel-gel interface (vertical dashed line in Fig. 4), whereas the hoop stretch function remains continuous owing to perfect bonding between the two gel layers. Nevertheless, the hoop stretch function becomes non-smooth at this interface. For systems with higher slip-link fractions in the outer layer ($\mathcal{K}^{(1)} = 0.1$, $\mathcal{K}^{(2)} = 0.9$), the radial stretch decreases with dimensionless radius R/R_{in} in gel 1, then exhibits a sudden discontinuous increase at the interface, before decreasing again. The hoop stretch increases with R/R_{in} in gel 1 and continues growing at an accelerated rate beyond the interface. Conversely, for systems with lower slip-link fractions in the outer layer ($\mathcal{K}^{(1)} = 0.9$, $\mathcal{K}^{(2)} = 0.1$), the radial stretch decreases with R/R_{in} in gel 1, then undergoes a discontinuous decrease at the interface followed by slight recovery. The hoop stretch increases

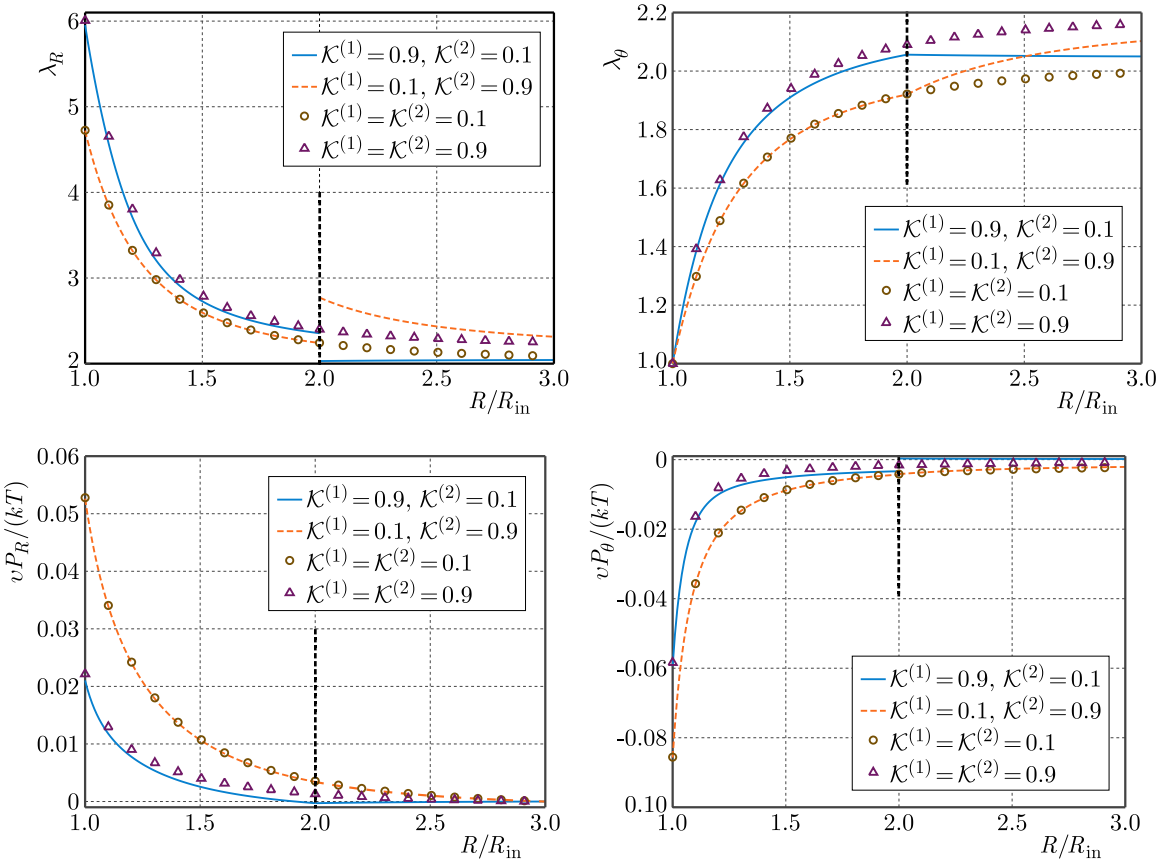

Fig. 4. Effects of slip-link fraction on the stretches (upper panels) and normalized stresses (lower panels) with $\alpha^{(s)} = 0.1$ and $\eta^{(s)} = 0.1$ for $s = 1, 2$.

with R/R_{in} in gel 1 but decreases beyond the interface. The stress distributions show distinct patterns. For $\mathcal{K}^{(1)} = 0.9$, $\mathcal{K}^{(2)} = 0.1$, the radial stress decreases with R/R_{in} in gel 1, transitions from tensile to compressive at the interface, then increases to zero at the outer surface. The hoop stress increases with R/R_{in} in gel 1, discontinuously changes from compressive to tensile at the interface, then decreases to zero at the outer surface. For $\mathcal{K}^{(1)} = 0.1$, $\mathcal{K}^{(2)} = 0.9$, both stress functions nearly coincide with the $\mathcal{K}^{(1)} = \mathcal{K}^{(2)} = 0.1$ case. Notably, the outer layer with a lower slip-link fraction exerts greater influence on the inner layer. Both stretch and stress functions in gel 1 show closer correspondence between cases $\mathcal{K}^{(1)} = 0.1$, $\mathcal{K}^{(2)} = 0.9$, and $\mathcal{K}^{(1)} = \mathcal{K}^{(2)} = 0.1$ compared to cases $\mathcal{K}^{(1)} = 0.9$, $\mathcal{K}^{(2)} = 0.1$, and $\mathcal{K}^{(1)} = \mathcal{K}^{(2)} = 0.9$.

The effects of the inextensibility parameter on mechanical behavior are opposite to those of the slippage parameter, as demonstrated in Fig. 5 and Fig. 6. Increasing the inextensibility parameter reduces stretches while amplifying stress magnitudes. Conversely, increasing the slippage parameter enhances stretches and diminishes stress magnitudes. Differences in inextensibility and slippage parameters between gel layers induce abrupt changes at the gel-gel interface. The upper panels of Figs. 5 and 6 reveal that dual-layer gel systems with lower inextensibility parameters or higher slippage parameters exhibit a sudden discontinuous increase in radial stretch at the interface, followed by a subsequent decrease, while the hoop stretch demonstrates accelerated growth beyond the interface. In contrast, systems with higher inextensibility parameters or lower slippage parameters display a sudden discontinuous decrease in radial stretch at the interface before recovery, accompanied by reduced hoop stretch beyond the interface. The lower panels of Fig. 5 and Fig. 6 reveal that gel systems with softer inner layers (characterized by lower inextensibility parameters or higher slippage parameters) exhibit a transition from tensile to compressive radial stress and from compressive to tensile hoop stress at the gel-gel interface. This behavior arises from the constraint imposed by the stiffer outer layer on the deformation

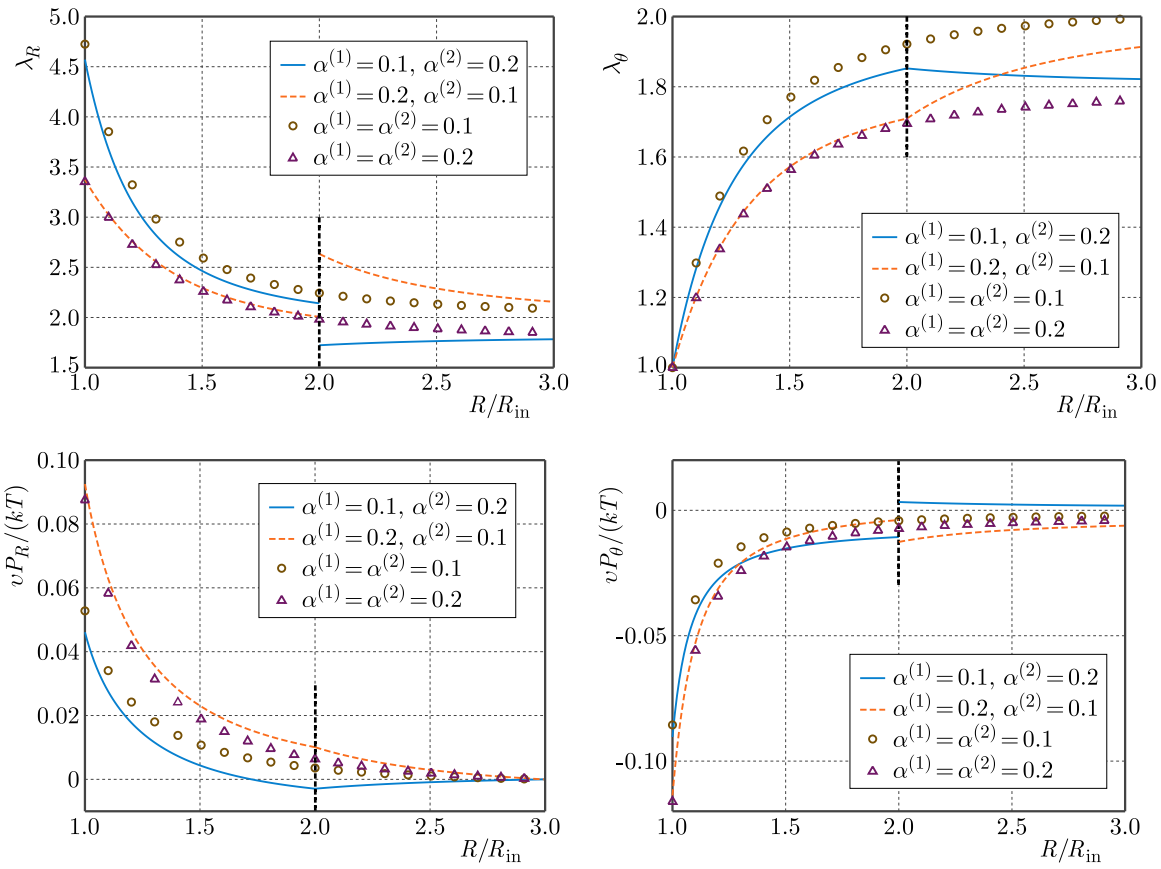

Fig. 5. Effects of inextensibility parameter on the stretches (upper panels) and normalized stresses (lower panels) with $\mathcal{K}^{(s)} = 0.1$ and $\eta^{(s)} = 0.1$ for $s = 1, 2$.

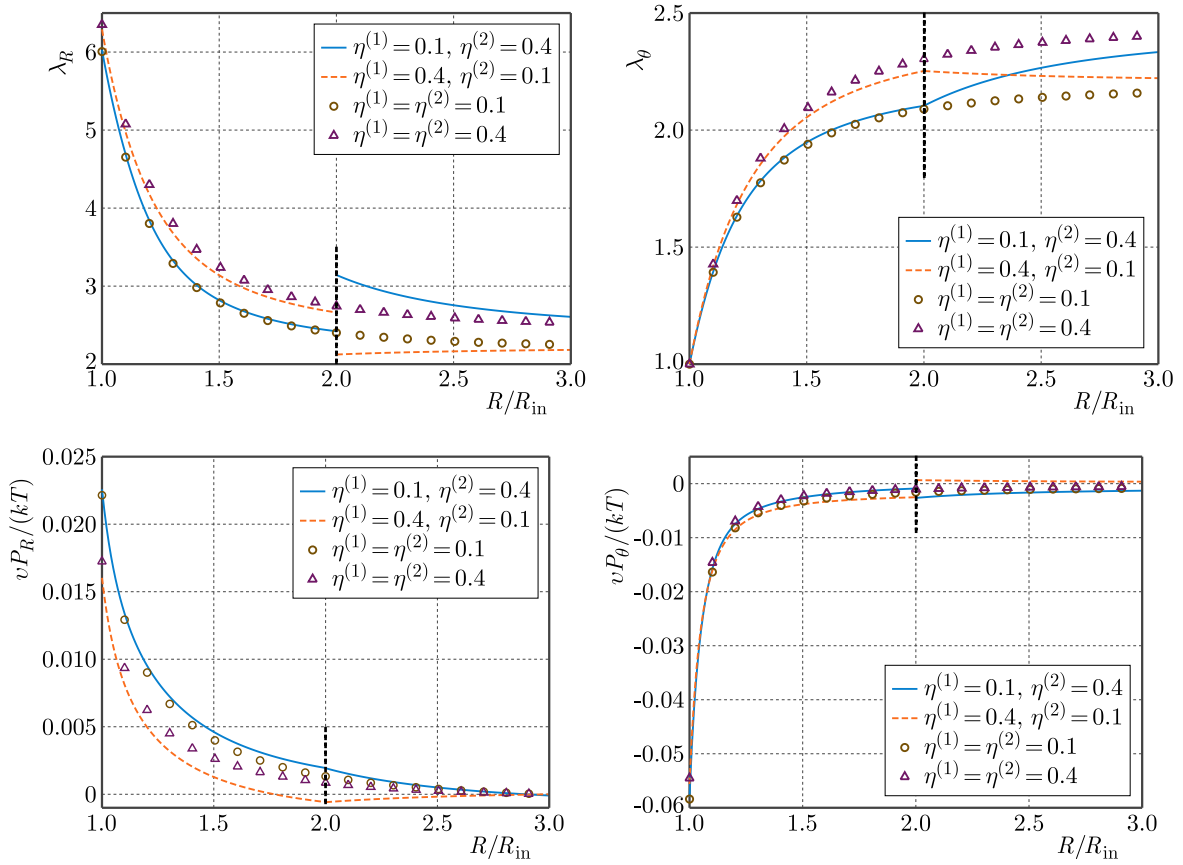

Fig. 6. Effects of slippage parameter on the stretches (upper panels) and normalized stresses (lower panels) with $\mathcal{K}^{(s)} = 0.9$ and $\alpha^{(s)} = 0.05$ for $s = 1, 2$.

of the softer inner layer. Conversely, systems with softer outer layers demonstrate an abrupt reduction in tensile radial stress and a sudden increase in compressive hoop stress, attributed to the enhanced deformation capacity of the softer outer layer. Both radial and hoop stresses approach to zero at the outer surface.

Figure 7 demonstrates the influence of micromaterial parameters on the solvent concentration distribution and equilibrium outer radius of the gel system. The left panels reveal that due to core constraints, solvent concentration increases with the distance from the core. The solvent concentration exhibits direct proportionality to the slip-link fraction and slippage parameter, while demonstrating inverse proportionality to the inextensibility parameter. Dual-layer gel systems with softer outer layers exhibit discontinuous increases in solvent concentration at the gel-gel interface, whereas systems with stiffer outer layers display the opposite behavior.

The equilibrium outer radius is crucial for various applications. We maintain a constant total thickness of the dual-layer gel, $(R_{\text{out}} - R_{\text{in}})/R_{\text{in}} = 2$, while varying the thickness ratio of the inner and outer layers, $\delta^{(1)}/\delta^{(2)}$, where $\delta^{(s)}$ represents the thickness of the s-th layer. The equilibrium outer radius is plotted as a function of the thickness ratio in the right panels of Fig. 7.

When micromaterial parameters are identical in both layers, the dual-layer gel system reduces to a single-layer gel system, and varying the thickness ratio does not affect the outer radius since the total thickness remains constant. Larger slip-link fractions and slippage parameters result in greater gel swelling, while the inextensibility parameter exhibits the opposite effect. For systems with softer inner layers, the outer radius increases with the thickness ratio, whereas systems with softer outer layers demonstrate the opposite trend. The variation range of the outer radius in dual-layer gel systems does not exceed that of single-layer gel systems. As the thickness ratio increases, the outer radius of dual-layer gel systems approaches that of the corresponding single-layer gel system.

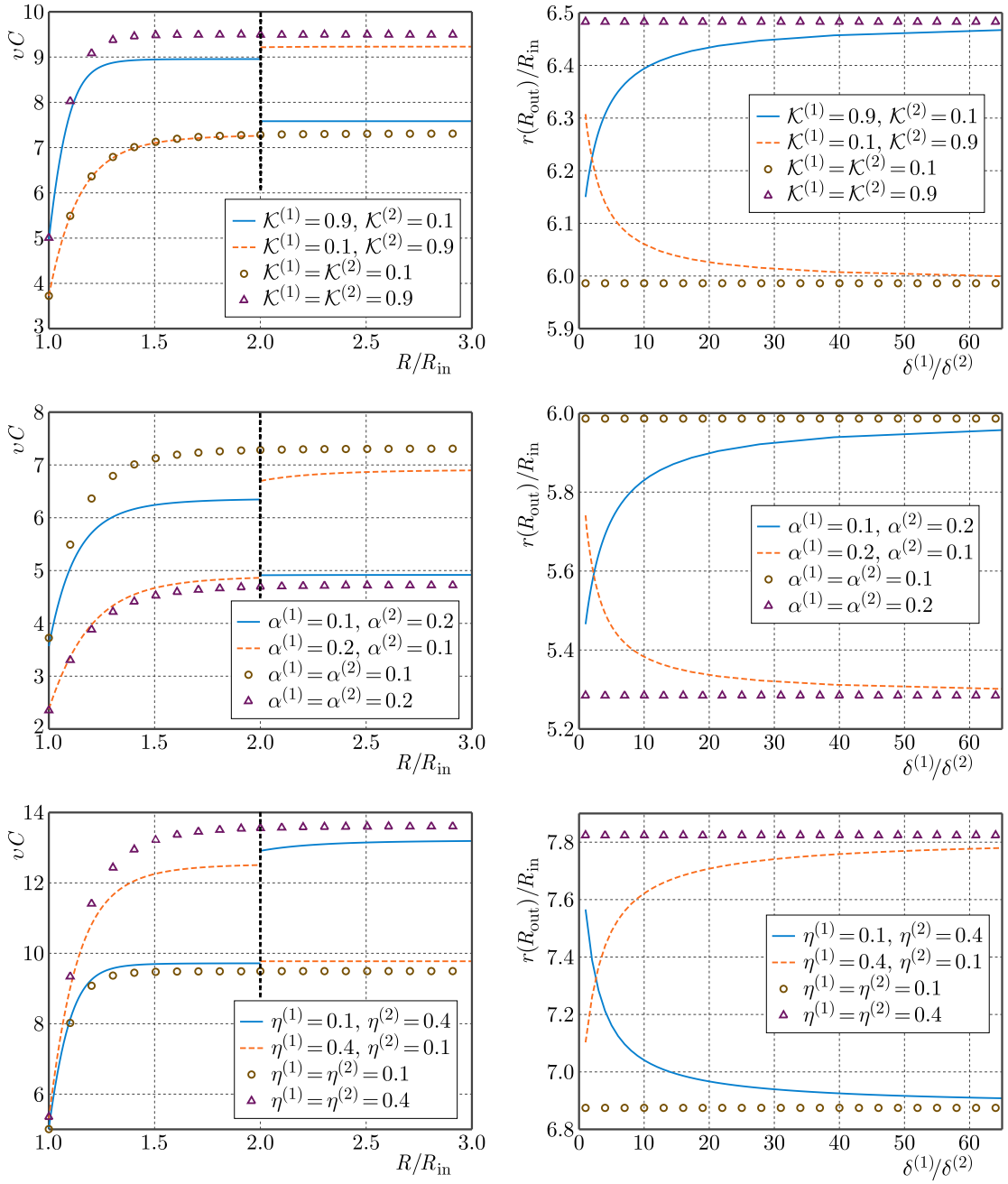

Fig. 7. Effects of slip-link fraction (upper panels, $\alpha^{(s)} = 0.1$ and $\eta^{(s)} = 0.1$ for $s = 1, 2$), inextensibility parameter (middle panels, $\mathcal{K}^{(s)} = 0.1$ and $\eta^{(s)} = 0.1$ for $s = 1, 2$), and slippage parameter (lower panels, $\mathcal{K}^{(s)} = 0.9$ and $\alpha^{(s)} = 0.05$ for $s = 1, 2$) on the distribution of solvent concentration (left panels) and outer radius of the gel system in equilibrium state (right panels).

5. Conclusion

This investigation presents a comprehensive theoretical and computational framework for analyzing the inhomogeneous swelling behavior of dual-layer spherical gels containing rigid cores. By incorporating the Edwards–Vilgis slip-link model, we successfully capture chain entanglement effects that are ubiquitous in actual gel networks but neglected by traditional Neo–Hookean formulations. The developed PINN methodology transforms the computational challenges of interface continuity conditions into an optimization problem, eliminating the need for iterative coupling procedures typically associated with interface problems, presenting a potentially more efficient computational paradigm for multi-domain or multi-physics applications.

Our systematic parametric analysis reveals that micromaterial parameters significantly influence mechanical behavior, stress distribution, and solvent concentration profiles. Notably, parameter disparities between gel layers induce discontinuous radial stretch distributions while maintaining interface continuity for hoop stretches. The outer layer exerts dominant influence on the inner layer's mechanical response. These findings establish a rigorous foundation for rational design and optimization of dual-layer gel systems, enabling precise control over target solvent concentrations, stress distributions, and equilibrium outer radii in dual-layer spherical gel systems. The framework advances fundamental understanding of dual-layer gel mechanics while providing practical tools for engineering applications in sensors, actuators, and drug delivery systems.

Acknowledgments

This work was supported by the National Science Foundation of China (12001172), the Natural Science Foundation of Fujian Province (2023J011031) and Joint Fund for Scientific and Technological Research and Development Plan in Henan Province (242103810029).

References

1. Abdolahi, J., Baghani, M., Arbabi, N., & Mazaheri, H. (2017). Finite bending of a temperature-sensitive hydrogel tri-layer: An analytical and finite element analysis. *Composite Structures*, *164*, 219–228. https://doi.org/10.1016/j.compstruct.2016.12.063
2. Ahmadi, M., Zholobko, O., & Wu, X.-f. (2020). Inhomogeneous swelling behavior of a bi-layered spherical hydrogel containing a hard core. *Journal of Applied Physics*, *128*(4), Article 044703. https://doi.org/10.1063/5.0016112
3. Ballauff, M., & Lu, Y. (2007). "Smart" nanoparticles: Preparation, characterization and applications. *Polymer*, *48*(7), 1815–1823. https://doi.org/10.1016/j.polymer.2007.02.004
4. Chester, S.A., & Anand, L. (2010). A coupled theory of fluid permeation and large deformations for elastomeric materials. *Journal of the Mechanics and Physics of Solids*, *58*(11), 1879–1906. https://doi.org/10.1016/j.jmps.2010.07.020
5. Diao, Y., Yang, J., Zhang, Y., Zhang, D., & Du, Y. (2023). Solving multi-material problems in solid mechanics using physics-informed neural networks based on domain decomposition technology. *Computer Methods in Applied Mechanics and Engineering*, *413*, Article 116120. https://doi.org/10.1016/j.cma.2023.116120
6. Edwards, S.F., & Vilgis, Th. (1986). The effect of entanglements in rubber elasticity. *Polymer*, *27*(4), 483–492. https://doi.org/10.1016/0032-3861(86)90231-4
7. Flory, P.J. (1942). Thermodynamics of high polymer solutions. *The Journal of Chemical Physics*, *10*(1), 51–61. https://doi.org/10.1063/1.1723621
8. Flory, P.J., & Rehner, J. (1943). Statistical mechanics of cross-linked polymer networks II. Swelling. *The Journal of Chemical Physics*, *11*(11), 521–526. https://doi.org/10.1063/1.1723792
9. Huggins, M.L. (1941). Solutions of long chain compounds. *The Journal of Chemical Physics*, *9*(5), 440. https://doi.org/10.1063/1.1750930
10. Jin, L., Xu, J., Xue, Y., Zhang, X., Feng, M., Wang, C., Yao, W., Wang, J., & He, M. (2021). Research progress in the multilayer hydrogels. *Gels*, *7*(4), Article 172. https://doi.org/10.3390/gels7040172
11. Khan, M.U.A., Stojanović, G.M., Abdullah, M.F.B., Dolatshahi-Pirouz, A., Marei, H.E., Ashammakhi, N., & Hasan, A. (2024). Fundamental properties of smart hydrogels for tissue engineering applications: A review. *International Journal of Biological Macromolecules*, *254*(Part 3), Article 127882. https://doi.org/10.1016/j.ijbiomac.2023.127882
12. López-Díaz, A., Vázquez, A.S., & Vázquez, E. (2024). Hydrogels in soft robotics: Past, present, and future. *ACS Nano*, *18*(32), 20817–20826. https://doi.org/10.1021/acsnano.3c12200

13. Morimoto, T., & Ashida, F. (2015). Temperature-responsive bending of a bilayer gel. *International Journal of Solids and Structures*, *56–57*, 20–28. https://doi.org/10.1016/j.ijsolstr.2014.12.009

14. Raissi, M., Perdikaris, P., & Karniadakis, G.E. (2019). Physics-informed neural networks: A deep learning framework for solving forward and inverse problems involving nonlinear partial differential equations. *Journal of Computational Physics*, *378*, 686–707. https://doi.org/10.1016/j.jcp.2018.10.045

15. Su, H., Yan, H., Zhang, X., & Zhong, Z. (2022). Multiphysics-informed deep learning for swelling of pH/temperature sensitive cationic hydrogels and its inverse problem. *Mechanics of Materials*, *175*, Article 104498. https://doi.org/10.1016/j.mechmat.2022.104498

16. Su, H., Yan, H., & Zhong, Z. (2021). Deep neural networks for large deformation of photo-thermo-pH responsive cationic gels. *Applied Mathematical Modelling*, *100*, 549–563. https://doi.org/10.1016/j.apm.2021.08.013

17. Urayama, K., Kawamura, T., & Kohjiya, S. (2003). Multiaxial deformations of end-linked poly(dimethylsiloxane) networks. 4. Further assessment of the slip-link model for chain-entanglement effect on rubber elasticity. *The Journal of Chemical Physics*, *118*(12), 5658–5664. https://doi.org/10.1063/1.1555636

18. Wu, Z., & Zhong, Z. (2013). Inhomogeneous equilibrium swelling of core-shell-coating gels. *Soft Materials*, *11*(2), 215–220. https://doi.org/10.1080/1539445x.2012.617644

19. Yan, H., & Jin, B. (2012). Influence of microstructural parameters on mechanical behavior of polymer gels. *International Journal of Solids and Structures*, *49*(3–4), 436–444. https://doi.org/10.1016/j.ijsolstr.2011.10.026

20. Yan, K., Xu, F., Wei, W., Yang, C., Wang, D., & Shi, X. (2021). Electrochemical synthesis of chitosan/silver nanoparticles multilayer hydrogel coating with pH-dependent controlled release capability and antibacterial property. *Colloids and Surfaces B: Biointerfaces*, *202*, Article 111711. https://doi.org/10.1016/j.colsurfb.2021.111711

21. Yang, J., Bai, R., Chen, B., & Suo, Z. (2020). Hydrogel adhesion: A supramolecular synergy of chemistry, topology, and mechanics. *Advanced Functional Materials*, *30*(2), Article 1901693. https://doi.org/10.1002/adfm.201901693

22. Zhao, X., Hong, W., & Suo, Z. (2008). Inhomogeneous and anisotropic equilibrium state of a swollen hydrogel containing a hard core. *Applied Physics Letters*, *92*(5), Article 051904. https://doi.org/10.1063/1.2840158

23. Zhao, Y.-D., Lai, J.-H., & Wang, M. (2021). 4D printing of self-folding hydrogel tubes for potential tissue engineering applications. *Nano LIFE*, *11*(04), Article 2141001. https://doi.org/10.1142/s1793984421410014

Manuscript received August 10, 2025; accepted for publication December 9, 2025; published online February 26, 2026.